ROYAL SOCIETY OF CHEMISTRY

PAPER

CrossMark
click for updates

Development of a multifunctional TiO$_2$/MWCNT hybrid composite grafted on a stainless steel grating†

Sara Cravanzola, Sagar M. Jain,‡ Federico Cesano,* Alessandro Damin and Domenica Scarano

Functional materials have a promising potential for the fabrication of new devices with improved properties to meet many requirements, including environmental issues. Along this idea, a multiphase structure made using a TiO$_2$/MWCNT hybrid nanoscaffold grafted on a metal grating (stainless steel type), acting as a strong, highly durable and heat/thermal inert support, is proposed. The method, consisting firstly of the fabrication of a porous scaffold *via* catalytic-CVD of a MWCNT forest on stainless steel, followed by the grafting of nanocrystalline TiO$_2$ *via* the sol–gel method and then calcination, is simple and effective. Morphology, structure and optical properties have been investigated using XRD, SEM, AFM, and HRTEM techniques as well as Raman and UV-visible spectroscopy, and porosity analysis. Interestingly, the TiO$_2$/MWCNT hybrid composite exhibits enhanced photocatalytic activity as compared to nanocrystalline TiO$_2$, obtained by adopting the same preparation. More interestingly, the hybrid system exhibits additional functionalities, such as magnetic, surface and optical properties. The multifunctional approach allows for the combination of enhanced photodegradation with magnetic properties, which can make the recovery of a solution from a photocatalyst easier. Furthermore, it will be shown that, by moving from MWCNT/stainless steel to TiO$_2$/MWCNT/stainless steel composites, the surface character changes from hydrophobic to hydrophilic in nature. Grafting on the stainless steel support allows for the addition of a broad range of features, including combined strength and corrosion resistance in aqueous solutions at ambient temperature, together with enhancement of electrical, optical and photocatalytic properties.

1. Introduction

Hybrid nanomaterials are of particular interest because of their improved properties and promising technological applications, including sensors and biosensors, electrical and optical devices, solar cells and photocatalysts.[1–7] As a matter of fact, the combined use of different nanostructures and nanophases to form hybrid and/or composite architectures, may allow for the fabrication of multifunctional materials, in which each constituent brings one or more properties, such as structural (*i.e.* strength, durability, and mechanical properties) and non-structural functions (*i.e.* electrical and thermal conductivity, sensing, and energy harvesting/storage properties). Accordingly, layered materials incorporated into polymers (metal–organic framework nanosheets) or consisting of intercalated

Department of Chemistry, NIS (Nanostructured Interfaces and Surfaces) Interdepartmental Centre and INSTM Centro Di Riferimento, University of Torino, Via P. Giuria, 7, 10125 Torino, Italy. E-mail: federico.cesano@unito.it

† Electronic supplementary information (ESI) available: Additional figures and material characterization (SEM/EDAX), N$_2$-adsorption/desorption isotherms, hydrophilic/phobic surface properties. See DOI: 10.1039/c5ra15003e

‡ Current address: sagarmjain@gmail.com

ferromagnetic layers (CoAl-based layered-double-hydroxides) allow for outstanding CO$_2$ separation from CO$_2$/CH$_4$ gas mixtures or thermoresponsive switching ability, respectively.[8,9] As far as photocatalysis is concerned, an enhanced photocatalytic performance for the photodegradation of methylene blue (MB) has been obtained using amorphous TiO$_2$/ZnO hybrid nanorods, as compared to pure components.[10]

Among the many constituents of the hybrid composites, TiO$_2$ and carbon nanotubes (CNTs) have attracted considerable attention because of their outstanding optical, photoelectrochemical and electronic properties.[11] Mixed-phase TiO$_2$-based composites show higher photoreactivity in comparison with pure materials, due to the formation of solid–solid interfaces that can improve: (i) charge transfer and spatial separation, and (ii) the reduction of electron–hole recombination and of interface defective sites that act as catalytic "hot spots".[12–16]

In fact, the incorporation of CNTs into the TiO$_2$ matrix can enhance the conductivity of the TiO$_2$ aggregates and facilitate faster electron transport across the TiO$_2$ network, thus minimizing charge recombination and ensuring high photoactivity. Moreover, the synergistic effect of activated carbon and TiO$_2$ has been shown for photocatalytic degradation of organic compounds.[17]

These are crucial points, as recently TiO$_2$ has been mainly used in the decomposition of toxic and hazardous organic pollutants in contaminated water and air, which are of great importance for both health and environmental protection.[18–23]

However, the high photocatalytic activity of the TiO$_2$ nanoparticles is not the sole requisite for practical applications because, for photocatalysis processes in liquid media, the separation of TiO$_2$ material from the water solution after irradiation is mandatory.[24] TiO$_2$ microaggregates (instead of very small and isolated particles) are preferred, because they make the separation of the photocatalyst from the reaction medium more effective.[25] Following many authors, several approaches to control the size/shape, porosity, agglomeration and nature of the TiO$_2$ nanoparticles and films have been adopted.[26–36] Among all investigated methods, template-based procedures look ideal for controlling and adjusting the TiO$_2$ texture because the pore sizes of the templating scaffold, where the material is under formation, can be accurately tailored.[37,38] In this regard, it has been observed that the surface roughness, the composition, the thermal, and the chemical stability of the substrate have a direct influence on the purity, crystallinity, mesostructural ordering and photocatalytic activity of the obtained TiO$_2$ films.[39] Industrially important support materials like stainless steel alloys have been investigated by a few groups.[39–43]

Along these themes, in this work a TiO$_2$/MWCNT/stainless steel AISI 304 grating composite is prepared by chemical vapor deposition of MWCNTs and by sol–gel synthesis of TiO$_2$. Although the growth of the MWCNTs on a stainless steel support, promoted by internal (*via* chemical etching) or external catalysts is not new,[44–49] it will be shown that the formation of the hybrid TiO$_2$/MWCNT scaffold on stainless steel exhibits unprecedented multifunctional properties.

The role of each component within the composite can be summarized as follows: (i) TiO$_2$ is the working photocatalyst, (ii) the multiwalled carbon nanotube (MWCNT) forest is acting as a nanostructured support and as a templating phase, and (iii) the stainless steel expanded metal grating acts as a heat/chemical resistant, durable and strong support. Moreover, it will be shown that, besides the above-mentioned properties, the porosity of the hybrid structures, as well as the inter-phase contacts, surface character and magnetic properties can be suitably exploited to design multifunctional materials.

The composite grating has been characterized using scanning electron microscopy (SEM), atomic force microscopy (AFM), Raman spectroscopy, transmission electron microscopy (TEM), X-ray diffraction (XRD), energy dispersive spectroscopy (EDS) and thermogravimetric analysis (TGA). The catalytic activity of the TiO$_2$/MWCNT/stainless steel composite grating has been investigated using UV-vis spectroscopy, following the degradation of methylene-blue (MB) under solar-like irradiation.

2. Experimental

2.1 Materials

Synthesis of MWCNTs on stainless steel expanded grating. Aligned MWCNTs, often called the "MWCNT forest", were obtained *via* the catalytic chemical vapor deposition (CCVD) process in a horizontal tube reactor (d_{tube} = 2.5 cm), using ferrocene as a catalyst, on 304 stainless steel gratings acting as substrates (having high temperature oxidation resistance) (Fig. S1, ESI†). Supports were placed in the middle of the quartz tube first and the temperature of the oven was increased up to 800 °C (heating rate: 20 °C min^{-1}) under N$_2$ gas flow (70 mL min^{-1}). Then a C$_2$H$_4$/H$_2$ gas mixture (100 mL + 25 mL) was introduced (total flow 90 mL min^{-1}) for 1 h, then the gas flow was switched to N$_2$ and the temperature reduced.

Synthesis of TiO$_2$ on the MWCNT steel composite. A TiO$_2$ sol–gel solution was first prepared starting from 7.04 mmol of Ti isopropoxide (TIP) in 25.4 mL of isopropyl alcohol (IPA) and concentrated HNO$_3$ (20 mmol) with the addition of 0.4 mL distilled water at about 50 °C under magnetic stirring. Then, the MWCNT/stainless steel gratings were dipped in the solution for 1 h at RT under stirring, dried at 80 °C and calcined at 400 °C in air for 1 h. Although a higher temperature would increase the crystallinity/photoactivity of the TiO$_2$ nanocrystals, the thermal treatment in air has been set to 400 °C to obtain nearly crystalline anatase nanoparticles, thus preventing the extensive oxidation of the MWCNTs. As a matter of fact, this is known from the thermogravimetric (TG) profile of the carbon nanotubes coming from a second sample grid, besides the phase quantifications of the hybrid material (*vide infra*), the products coming after complete oxidation are obtained.

2.2 Methods

The structure and the morphology of the as-grown CNTs were investigated using Raman spectroscopy, scanning electron microscopy (SEM), and atomic force microscopy (AFM), while the TiO$_2$/MWCNT hybrid system was investigated using scanning and transmission electron microscopies. The Raman spectra were acquired using a micro–Raman Renishaw spectrometer equipped with a CCD detector. The 514 nm (green) and 785 nm (red) laser lines were used to excite the samples. All the measurements were performed at room temperature on the as-grown CNTs grafted on the support metal grating. The SEM images were taken on a Zeiss Evo 50 SEM instrument operating at 30 kV, the AFM images with a Park Systems XE-100 in non-contact mode, and the TEM images with a JEOL 3010-UHR instrument operating at 300 kV and equipped with a $2k \times 2k$ pixel Gatan US1000CCD camera.

The photodegradation experiments of methylene blue (MB) have been followed using UV-vis spectroscopy (Varian Cary UV 5000) to assess the TiO$_2$/MWCNT hybrid system grafted to the metal grating, the as-prepared TiO$_2$ and TiO$_2$ (P25) centrifuged solutions (used as a reference system). The gradual disappearance of the bands of MB adsorbed on the different systems upon exposure to visible light for increasing amounts of time was investigated. Photoluminescence (PL) spectra have been obtained at RT using an excitation incident light of 325 nm, coming from a conventional Xe arc lamp (HORIBA Jobin Yvon Fluorolog-3 instrument). To minimize reflections of the incident light, samples have been placed at 15° from the specular direction.

X-ray diffraction patterns of samples have been collected with a diffractometer (PANalytical PW3050/60 X'Pert PRO MPD) using a Ni-filtered Cu anode and working in Bragg–Brentano geometry. Qualitative phase identification from the XRD data is based on the International Center for Diffraction Data (ICDD) powder diffraction files.

Weight ratios of TiO_2/MWCNTs have been obtained from the TG curve profile of the TiO_2/MWCNT hybrid material, scratched away from the second steel substrate, which has also been thermally treated up to 800 °C in N_2 gas flow first. Then, during subsequent isothermal treatment (800 °C) the gas flow has been switched to air. The observed residual weight (≈ 25 %wt) and weight loss (≈ 75 %wt) are associated with the TiO_2 amount and with the MWCNT quantity after complete oxidation, respectively (Fig. S6, ESI†). In a second experiment, total weight of the MWCNTs on the steel grids, and hence the total amount of the TiO_2 phase, has been obtained from the weight analysis of the second sample before and after thermal oxidation (800 °C).

N_2 adsorption–desorption experiments have been carried out at 77 K (Micromeritics ASAP 2020 instrument) to determine the Brunauer–Emmett–Teller (BET) surface area and the micropore volume (t-plot method). A powder sample was gently scratched from the TiO_2/MWCNT composite, while the TiO_2 sample was investigated as obtained. The surface area of the samples was determined after outgassing at 150 °C overnight. The pore size distributions (PSDs) were obtained using a non-negative least squares fitting of the absorption isotherm data by applying the Density Functional Theory (DFT) method (NLDFT model, cylinder as a geometry) with ASAP 2020 4.0 software (Micromeritics). Microporous (S_{micro}) and mesoporous (S_{meso}) surfaces were obtained from the t-plot method (Harkins and Jura thickness curve) and from $S_{meso} = S_{tot} - S_{micro}$, respectively.

Photodegradation test. The TiO_2/MWCNT/stainless-steel grating and the powder samples (5.1 mg TiO_2 coming from sol–gel preparation, together with 5.1 mg P25 TiO_2) were dispersed in separated aliquots (8.5 mL) of a methylene blue (MB) water solution (12.5 mg L^{-1}). Then the samples were kept in the dark at RT for 1 hour. After exposure to a solar lamp, MB–as-prepared TiO_2 and MB–P25 TiO_2 dispersions were centrifuged at 10 000 rpm for 20 min.

Photocatalytic degradation of MB has been investigated using UV-vis spectroscopy. The solar light simulating irradiation was carried out at 25 °C ± 5 using a SOL2/500S lamp (Honle UV technology, Munchen, Germany). The SOL-bulb and the H_2 filter together yield a spectrum, which is very similar to natural sunlight, ranging from ultraviolet to infrared radiation ($\sim$295–3000 nm). The integrated intensity of the adsorbed MB manifestations (C) was used to obtain C/C_0 vs. time plots, where C_0 is the concentration, corresponding to the initial intensity before illumination. A comparative photodegradation test of the TiO_2/MWCNT/grating system and of the P25 reference TiO_2 powder has also been performed for several cycles (six cycles). After each cycle, samples have been magnetically extracted and dried (TiO_2/MWCNT/grating system) or obtained after filtering and drying the nanopowder (P25).

3. Results and discussion

## 3.1 Morphology and structure of the TiO_2/MWCNTs grafted on stainless steel

The structure and the composition of the TiO_2/MWCNT hybrid nanostructures on the stainless steel expanded metal grating are schematized in Scheme 1.

The multiphase system was obtained starting from a stainless steel support (Scheme 1a) (see SEM and EDAX analyses of the steel support in Fig. S1, ESI†), which first was used as a substrate to grow densely packed MWCNTs (Scheme 1b, step 1). Then, the MWCNT-covered stainless steel grating was dipped in a sol–gel solution containing the TiO_2 precursor and calcinated at 400 °C to obtain the final TiO_2/MWCNT/steel multiphase structure (Scheme 1c, step 2).

XRD diffraction measurements have been performed to follow the preparation steps as described in Scheme 1 (Fig. 1). In particular, Fig. 1 compares patterns of: (a) the untreated support, (b) the MWCNT forest/stainless steel composite, (c) the MWCNT forest/stainless steel composite after impregnation with a TIP sol–gel solution and after thermal treatment at 400 °C, and (d) the pure powder obtained using the same sol–gel method for MWCNT/TiO_2 composites.

In more detail, moving from the (a) pattern of the stainless steel (face-centred cubic phased Fe; γ-Fe) (PDF card #65-4150) to that of the MWCNT/metal grating composite (pattern b), the complex envelope observed in the $2\theta = 35$–55° interval is best matched by the cementite phase (Fe_3C, PDF card #35-0772) with the contribution of the small features at $2\theta = 51°$ and $2\theta = 74.6°$ due to γ-Fe (austenitic stainless steel). Furthermore, the main peak around $2\theta = 26.2°$ in the same pattern is due to the (002) crystalline planes of the graphite phase (PDF card #41-1487). On the basis of this figure, from the small FWHM (about 0.93°) of the (002) diffraction peak, a high graphitisation degree of the MWCNTs covering the grating can be singled out.

From the XRD feature located at 44.7°, which can be indexed with the (110) plane reflections of α-Fe (PDF #06-0696) and then confirmed from the Fe–C phase diagram, the contribution of the body-centred cubic phase of α-Fe is inferred. The possible
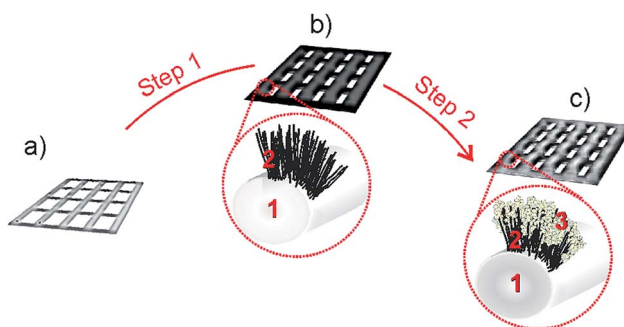
Scheme 1 Preparation steps to fabricate the hybrid TiO_2/MWCNT/steel structure. Step 1: synthesis of the MWCNTs on the stainless steel grating. Step 2: grafting of the nanocrystalline TiO_2 nanoparticles on the MWCNT support via the sol–gel method and calcination at 400 °C. The multiphase structure is also schematized: 1-stainless steel grating; 2-MWCNT forest and 3-nanocrystalline porous TiO_2 layer.
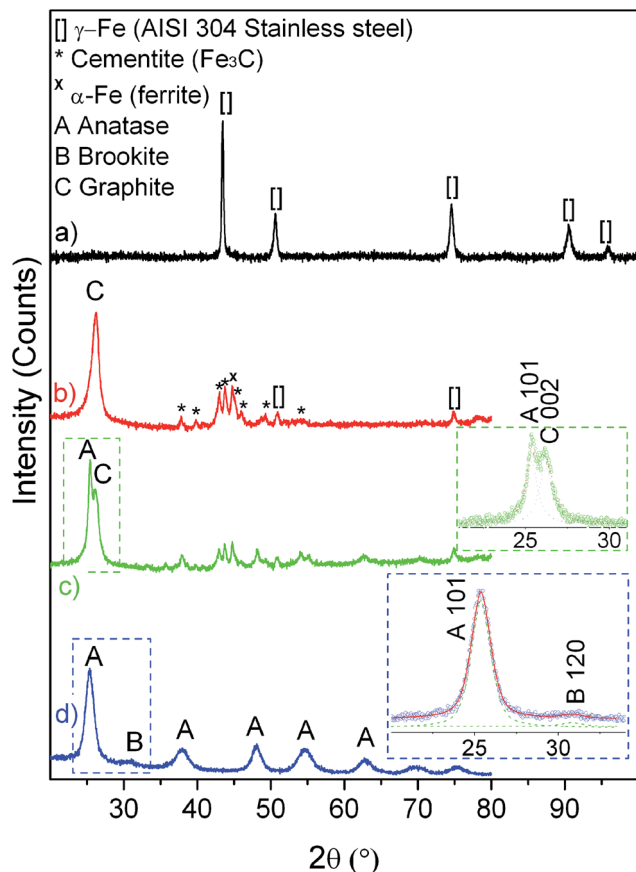
Fig. 1 XRD patterns of: (a) the stainless-steel grating used as a support, (b) the MWCNT/metal grating composite, (c) the MWCNT/metal grating composite after impregnation with a TIP sol–gel solution and thermal treatment at 400 °C for 1 h in air, and (d) the pure powder obtained from the sol–gel solution treated at the same temperature (400 °C). XRD line positions of the standards are reported for comparison: (A) anatase (PDF card #21-1272), (B) brookite (PDF card #29-1360), (C) graphite (PDF card #41-1487), (*) cementite (Fe₃C, PDF card #35-0772), ([]) γ-Fe (AISI 304 stainless steel) (fcc-phased Fe, PDF card #65-4150) and α-Fe (ferrite, bcc-phased Fe, PDF card # 06-0696) (X), respectively.

(101) anatase crystalline planes, nanocrystals of about 6 nm in size are obtained.

3.2 Morphology and structure of the MWCNTs grafted on a stainless steel metal grating

The carbon nanotube forest, obtained on the grating by catalytic decomposition of C_2H_4 at 800 °C for 1 h, was imaged using SEM and AFM, as shown in Fig. 2. The low resolution top-view SEM images (Fig. 2a and the inset therein) illustrate that the carbon nanotubes are entirely covering the support, thus reducing the size of the cavities, which locally appear to be completely obstructed. From the high-resolution SEM image (Fig. 2b) densely packed carbon nanotubes, with lengths ranging from 25–50 μm and protruding from the supporting grating, are shown. As no details are obtained at the nanometer scale on the emerging network of the CNTs, more insights come from AFM analysis (Fig. 2c). From this, it is shown that the emerging CNTs, about 20–30 nm in diameter, are vertically oriented. In addition, within the dense CNT forest, pores about 20–60 nm in diameter can be highlighted at the adopted resolution.

Raman spectroscopy provides an accurate investigation of the properties of the carbon-based materials, thus giving information on purity, structure, defectiveness and any presence of amorphous carbon phases. All graphite-like materials, including MWCNTs, show a strong peak in the first-order Raman spectra, around 1580 cm^{-1} (G-band), which is the high-frequency E_{2g} first-order mode. Additional features in the first-order Raman spectra, such as the D-band, around 1300–1350 cm^{-1}, and D′-band at about 1620 cm^{-1}, are associated with more disordered phases (amorphous carbon) and exhibit dispersive behaviour, as these frequencies change as a function of laser energy.[53–55] In particular, frequencies upshift linearly with increasing excitation energy over a wide laser energy range. In the second-order region of the Raman spectra the main fingerprints in the 2650–2750 cm^{-1} interval (G′-band), are caused by two-phonon scattering around the K point of the Brillouin zone, which are again sensitive to increasing defect density.

Raman spectra obtained with $\lambda = 514$ nm and $\lambda = 785$ nm laser line excitation are shown in Fig. 2d. The green spectrum ($\lambda = 514$ nm) shows three distinct, well defined bands, with maxima at 1356 cm^{-1} (D-band), 1585 cm^{-1} (G-band) and 2708 cm^{-1} (G′-band), while the red spectrum ($\lambda = 785$) shows a more complex situation.

As a matter of fact, in the red spectrum, besides the two downward shifted bands at 1313 cm^{-1} (D-band) and 2624 cm^{-1} (G′-band), a more complex envelope with two maxima at 1586 cm^{-1} (G-band) and at 1612 cm^{-1} (D′-band) can be observed.

Although detailed discussion of these spectra is beyond the scope of this paper and the reader can be referred elsewhere,[56] some fingerprints merit discussion. Beyond the general assignment, it is worth noticing that in the Raman spectrum obtained by 785 nm laser line excitation, the weak D′-band disorder-induced feature, which is silent under 514 nm illumination, is observed at 1612 cm^{-1}.

conversion of Fe during thermal treatments or the synthesis of CNTs is documented in some papers.[45,50–52] In Fig. 1c and in the corresponding inset, the $2\theta \approx 24.6°–25.6°$ feature, due to the formation of the TiO_2 phase (anatase), is also observed. From this, the simultaneous presence in the composite of graphite and anatase (PDF card #21-1272) phases can be highlighted, as compared with the pattern of the TiO_2 pure powder obtained from the sol–gel solution (Fig. 1d). Notice a further small contribution due to the weak and broad feature at $2\theta = 30–33°$, which can be indexed with the (121) XRD reflection planes of brookite (PDF card #29-1360) (Fig. 1d).

From Scherrer's equation ($L = K\lambda/\beta \cos \theta$, where λ is the X-ray wavelength, β is the FWHM of the diffraction line corrected by instrumental broadening, θ is the diffraction angle, and K is a constant, which has been assumed to be 0.9), the mean crystallite size of the anatase particles was calculated. More precisely from the $2\theta = 25.4°$ XRD peak (Fig. 1d), assigned to the
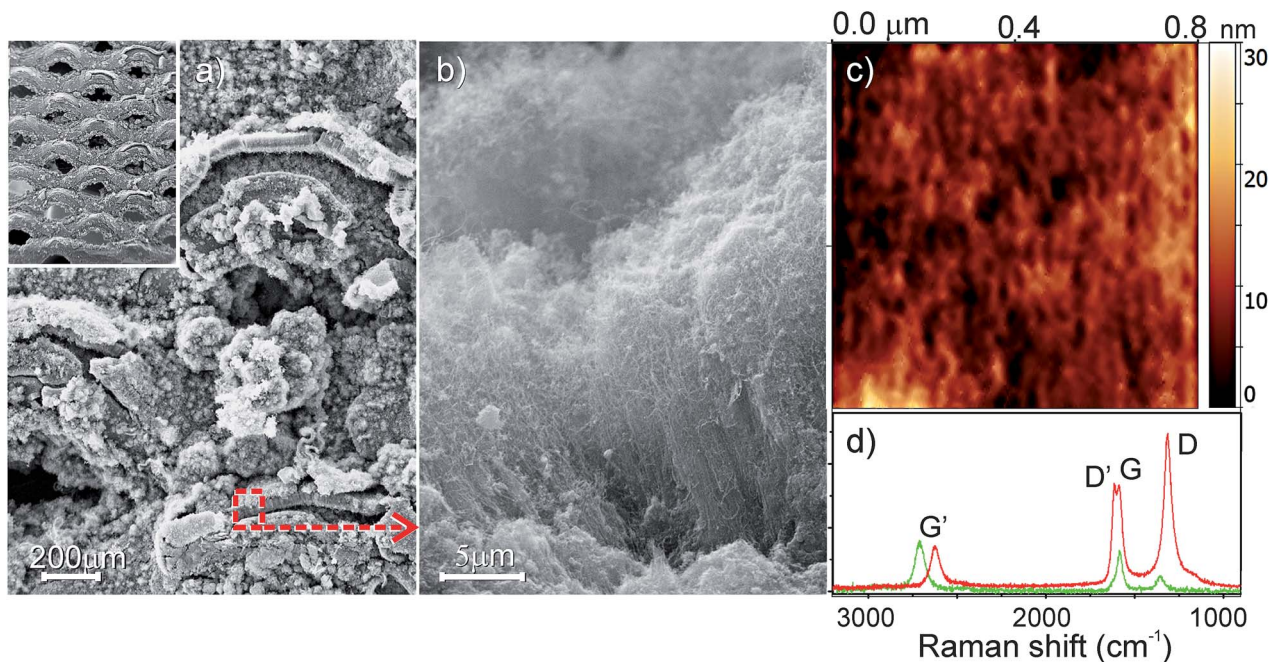
Fig. 2 (a) Top-view SEM images of the stainless steel grating after CNT growth; (b) enlarged view of a selected area on (a) the SEM image; (c) top-view 0.8 × 0.8 μm nc-AFM image of the emerging network of CNTs; (d) μ-Raman spectra of the MWCNTs obtained by λ = 514 nm and λ = 785 nm laser line excitations (green and red spectra, respectively).

Notice that, in agreement with literature data, the G peak is quite independent of excitation wavelengths. Conversely the D, D′ and G′ bands downshift with increasing wavelength and their relative intensity increases. These phenomena can be explained by the double resonance theory.[57]

Moreover, as D′ bands become as intense as the G-band for excitation wavelengths in the infrared region, it is considered distinctive of densely aligned and vertically oriented MWCNTs, which are grown perpendicular to the substrate,[58,59] in agreement with our structural model. In addition, the observed small line-widths indicate that these features are representative of high quality MWCNTs with a very good structural order.[58]

In conclusion, we state that the synthesis of the MWCNT forest on the stainless steel support with an external catalyst is more effective as compared to the same process without the external catalyst, as reported in the literature.[44–49]

3.3 Morphology, structure and properties of the TiO₂/MWCNT/stainless steel metal grating composite

The morphology and the structure of the TIP impregnated MWCNTs/stainless steel, after calcination in air at 400 °C, are SEM and TEM imaged, as shown in Fig. 3. From the low resolution top-view SEM images (Fig. 3a and b and the inset therein) an envelope of many aggregated particles can be highlighted, which identifies a highly compact network of carbon nanotubes.

Information about the structure at the nanoscale comes from the HRTEM image of the composite, where the interphase between a carbon nanotube and TiO_2 nanoparticles is shown in Fig. 3c. In particular, besides a MWCNT having about 40 walls, TiO_2 nanocrystals about 5–6 nm in size are observed, whose crystalline nature is testified by the presence of well-defined interference fringes 0.35 nm spaced, which correspond to the (101) anatase crystalline planes.

A different region, far from the TiO_2/MWCNT interphase, is imaged using HRTEM and shown in Fig. 4a, together with the corresponding filtered image (Fig. 4b), where highly crystalline TiO_2 nanoparticles are seen. Moreover, from the unfiltered and filtered inverse fast-Fourier transforms (IFFTs) of the selected region (insets respectively in Fig. 4a and b), the nanoparticle domains have been identified.

In fact, from the interference fringes on the filtered image (Fig. 4b), obtained by selecting almost all the spots of the filtered inverse fast-Fourier transform (IFFT) (inset in Fig. 4b), domains ranging from 5–10 nm can be easily estimated.

Notice that mean sizes of about 6 nm have been obtained for TiO_2 nanoparticles, using Scherrer's equation from XRD measurements. More details concerning the diffraction planes can be obtained from the HRTEM image (Fig. 4c) of a selected TiO_2 nanoparticle (dotted square in Fig. 4a).

Well-defined interference fringes, 0.35 nm and 0.19 nm spaced, corresponding respectively to the {101} and {200} anatase planes, are found. From the FFT pattern (Fig. 4d) and from the corresponding simulated electron diffraction pattern (Fig. 4e) of the selected region, the anatase [0,1,0] zone-axis direction is obtained.

The optical properties of the TiO_2/MWCNT/stainless steel composite and of the TiO_2 powders, obtained by the same sol–gel method used for MWCNT/TiO_2 composites, have been investigated using UV–vis spectroscopy in the reflectance mode (DR) and the results obtained in the 28 000–23 500 cm⁻¹ interval are shown in Fig. 5. In the same figure the spectrum of
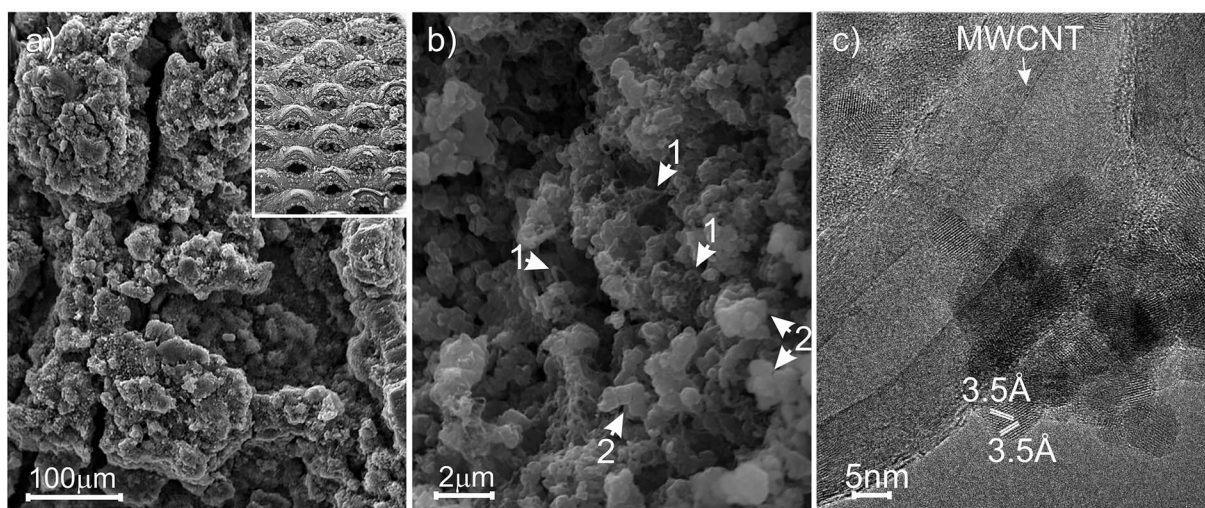
Fig. 3 (a) Top-view SEM images of the TIP impregnated MWCNT/stainless steel metal grating after thermal treatment at 400 °C; (b) enlarged view of a selected area from the SEM image in (a); (c) HRTEM image of a CNT–TiO₂ junction region.
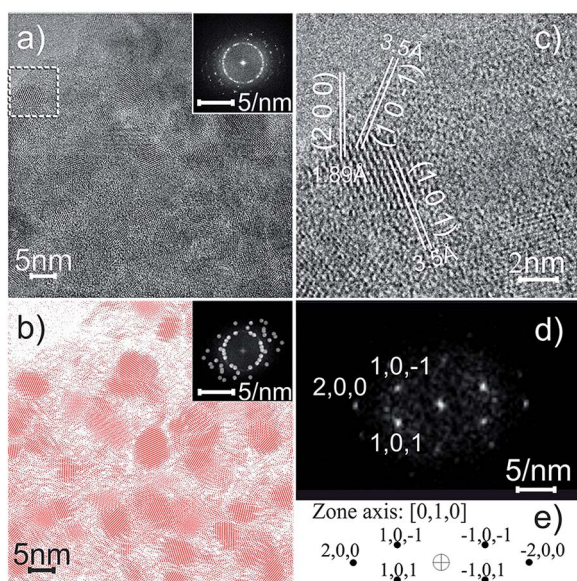

Fig. 4 (a) HRTEM image of a region of the TiO₂/MWCNT/metal grating composite (inset: unfiltered inverse fast-Fourier transforms, IFFT); (b) HRTEM filtered image of (a) (inset: filtered inverse fast-Fourier transforms IFFT); (c) HRTEM image of a selected region in (a); (d) experimental IFFT image oriented along the [010] zone axis; (e) simulated SAED pattern, as obtained from the experimental IFFT image.

the reference material (P25 TiO₂) is reported for the sake of comparison.

From this figure, it can be inferred that the absorption edges of the TiO₂/MWCNT/stainless steel composite (circles) and of the as-prepared TiO₂ nanopowder (squares) are slightly red- and blue-shifted, respectively, with respect to that of P25 TiO₂ used as a reference material (dark triangles). The observed absorption edge of the as-prepared TiO₂-based material is in agreement with the small dimensions (3–10 nm) of the anatase nanoparticles with respect to those of P25. Besides, the

observed adsorption edge of P25 reflects the simultaneous presence of the anatase and rutile TiO₂ nanocrystals, 10–30 nm and ∼15–30 nm in size, respectively. It is worth noticing that the more appreciable red shift observed for the TiO₂ hybrid composite material, which is mainly due to the ascertained presence of the MWCNTs in the composite grating, may play a positive role in the adsorption of visible light, to be used for photocatalysis or photodegradation applications.

From the comparison of the volumetric N_2-adsorption/desorption isotherms of the TiO₂/MWCNT hybrid and of the pure TiO₂ material obtained by the same sol–gel method used for MWCNT/TiO₂ composites (Fig. S2, ESI†), the BET surface area (S_{BET}) and the micropore, mesopore and total pore volume of the two samples are obtained, as reported in Table 1. From the shapes of the adsorption/desorption branches a mixed
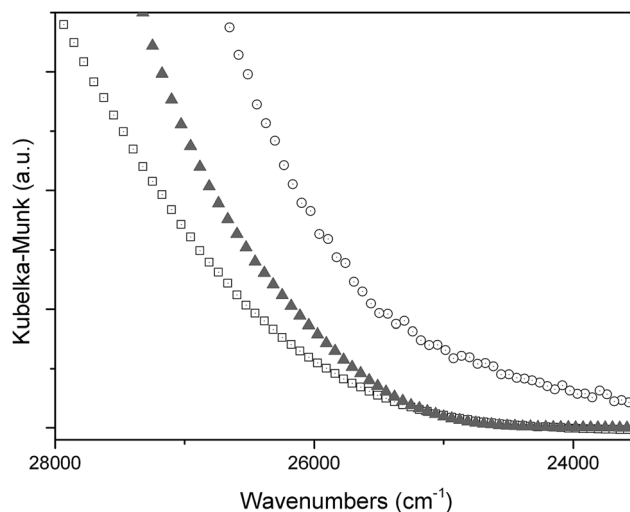

Fig. 5 UV-vis diffuse reflectance spectra of TiO₂/MWCNTs/stainless steel (○), pure TiO₂ powder obtained by the same sol–gel method used for MWCNT/TiO₂ composites (□), and P25 TiO₂ (▲).

microporous/mesoporous character is inferred for the $TiO_2/MWCNT$ hybrid structure, while the pure TiO_2 is essentially mesoporous. Further differences can be highlighted from the shape and location of the hysteresis loops.

More specifically, the pure TiO_2 material is dominated by a mesopore contribution in the 40–90 Å range, while the pore size distribution of the $TiO_2/MWCNT$ hybrid structure is much more complex. In fact the $TiO_2/MWCNT$ hybrid structure shows a micropore family in the 8–20 Å range (presumably arising from MWCNTs) and a wide and complex distribution of mesopores ranging in 20–50 Å, 50–100 Å, 150–200 Å and >250 Å intervals. These results are in agreement with the pore size distribution (PSD) obtained using the DFT model (Fig. S2b, ESI†) and by Barrett–Joyner–Halenda (BJH) analysis (data not shown for the sake of brevity). It is worth noticing that the complex pore evolution of the $TiO_2/MWCNT$ nanostructures, forming a hybrid porous scaffold, may play a role in photodegradation processes.

The porous character of the TiO_2-based materials looks ideal to test the photocatalytic degradation of methylene blue. Dimensions of MB along the main perpendicular directions (obtained as nucleus–nucleus distances) are reported in Fig. S3 (ESI†). Photodegradation experiments were performed by measuring, in water solutions, the decrement of the MB concentration adsorbed on the $TiO_2/MWCNT$ composite grating and on the samples containing the same quantity of photocatalysts (as prepared nanocrystalline TiO_2 and P25 TiO_2) upon light exposure for increasing amounts of time (Fig. 6).

The MB band evolution on the $TiO_2/MWCNT$/stainless steel composite, as a function of the exposure time under visible light, is shown in Fig. 6a. From this figure, it is shown that the intensity of the two main MB bands at 15 100 cm^{-1} (∼662 nm) and at 16 450 cm^{-1} (∼608 nm), which are assigned to monomeric and aggregated species,[5,60] decreases with the exposure time. Depending on the concentration, MB in solution may show a distinct tendency to form agglomerates, made by monomeric and polymeric species in thermodynamic equilibrium. Even though a detailed assignment of these bands is outside the scope of this work and can be found elsewhere,[61] the MB photodegradation performances of the $TiO_2/MWCNT$/stainless steel composite is compared to TiO_2 nanoparticles arising from the same temperature treatment (TiO_2@400 °C) and to the P25 TiO_2 photocatalyst (Fig. 6b).

At this point, notice that the photodegradation of the anatase nanoparticles grafted on the MWCNT scaffold is greater than of TiO_2@400 °C, but less than of P25. According to the
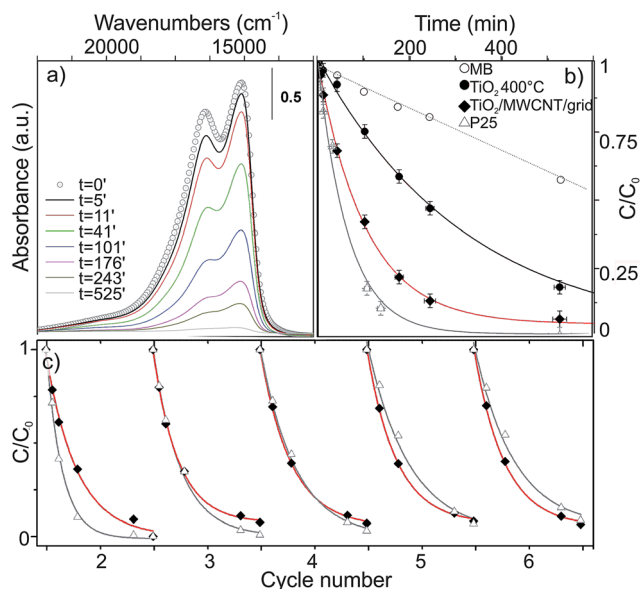

Fig. 6 (a) Evolution of UV-visible spectra of MB (water solutions) adsorbed on a $TiO_2/MWCNT$/stainless steel composite as a function of exposure time under visible light (0, 5, 11, 41, 101, 176, 243 and 525 min); (b) time dependence upon light exposure of a pure MB surface concentration (C/C_0) (^), of MB adsorbed on a $TiO_2/MWCNT$/metal grating composite (◆) as compared to MB adsorbed on as-prepared TiO_2 (●) and on TiO_2 P25 reference material (△); (c) performance in a cyclic photocatalytic test of the magnetically guided $TiO_2/MWCNT$/metal system (◆) as compared to P25 nanopowder (△).

literature, the photocatalytic/photovoltaic enhanced performance of TiO_2 due to the presence of carbon nanotubes is still under debate.[13,62–64] One of the most recognized explanations is that electron transport is accelerated by MWCNTs, which can accept electrons from photoexcited TiO_2. The resulting photoluminescence intensity has been found to be quenched.[65] The PL quenching efficiency, which has been demonstrated to be proportional to the fraction of nanotubes mixed with TiO_2 nanoparticles,[66] has also been verified for the $TiO_2/MWCNT$/steel composite with respect to the discrete TiO_2 nanoparticles, obtained at the same temperature (Fig. S4, ESI†). Due to its higher crystallinity and phase composition, P25 TiO_2 is, however, more photoactive than the hybrid material.

The hybrid composite system and the reference TiO_2 nanopowder (P25) have been tested in a continuous photocatalytic test performed for several cycles (Fig. 6c). Although the photodegradation activity of the hybrid photocatalyst is initially lower

Table 1 Surface area and porosity properties

	S_{BET}[a] (m^2 g^{-1})	S_{micro}[b] (m^2 g^{-1})	S_{meso}[b] (m^2 g^{-1})	% (S_{micro})[c]	V_{tot}[d] (cm^3 g^{-1})
$TiO_2/MWCNT$ hybrid scaffold obtained from the composite grating@400 °C	168	30	138	∼18%	0.3946
TiO_2@400 °C	146	—	146	100%	0.1453

[a] Evaluated in the $0.1 < P/P_0 < 0.3$ pressure range. [b] Estimated using the t-plot method (Harkins and Jura thickness curve). [c] % (S_{micro}) = S_{micro}/S_{BET} × 100. [d] Total pore volume (V_{tot}) calculated as the volume of the liquid at $P/P_0 \gg 0.975$.

in comparison with P25, its photoactivity is preserved. On the contrary the P25 efficiency is progressively reduced, becoming lower than that of the hybrid material after the first number of cycles. Hence the photodegradation of MB by TiO₂/MWCNT/ steel composite has been shown to be very effective.

In conclusion, it is shown that the MWCNT forest can have a role: (i) in reducing the recombination rate of the photo-generated electron–hole pairs due to the intimate contact between TiO₂ and MWCNTs, (ii) in extending the frequency values in the visible range (CNTs act as a photosensitizer), (iii) in acting as a dispersing agent, (iv) in inducing synergistic effects, and (v) in increasing the porosity of the material. The discussion of which of these factors is prevailing in our hybrid system goes beyond the scope of the present report. However, on the basis of our results a relevant role is played by MWCNTs in promoting the formation of a mesoporous scaffold.

Although the 304 austenitic stainless steel is expected to be only weakly ferromagnetic, notice that the obtained TiO₂/ MWCNT/stainless steel composite shows magnetic properties when a permanent magnet approaches (Fig. 7). The composite grating, placed in a glass beaker containing a MB water solution, can be moved by an external magnet, while dye photo-degradation under solar light is occurring.

It is known that, upon thermal treatment of the austenic stainless steel, the iron remains in the form of austenite (fcc-phased Fe, γ-Fe) also stimulated by the presence of nickel, acting as a stabilizer. However, the magnetic properties of the austenitic stainless steel can be modified by annealing/cooling steps, as well as by the growth of the MWCNTs.[51] Carbon nanotubes can selectively extract iron (and not nickel) from the support to form α-Fe (bcc phase). α-Fe is magnetic and stable up to very high temperatures ($\approx 900\,^\circ$C). Moreover, by moving from MWCNT to TiO₂/MWCNT hybrid scaffolds, the surface properties change from a hydrophobic to hydrophilic character (Fig. S5, ESI†). It has emerged that processes, like water

purification, can take advantage of both the magnetic and the surface properties of the MWCNT/stainless steel based composites. Hence the photodegradation of MB by a magneti-cally driven TiO₂/MWCNT/steel composite has been shown to be very effective in a practical routine due to its recyclability. By following the literature, magnetically guided titania nanotubes have been proposed for site selective photocatalytic processes and drug release applications.[67]

4. Conclusions

In summary, a simple method for fabricating multifunctional nanostructured material, to be used for the efficient and convenient photodegradation of dyes in solution, is reported. TiO₂/MWCNT hybrid structures, grafted on a stainless steel support, have been obtained by catalytic chemical vapour deposition of a dense forest of vertically oriented MWCNTs followed by grafting of nanocristalline anatase TiO₂. Carbon nanotubes are entirely covering the stainless steel metal and form a porous scaffold, which acts as a templating phase for grafting TiO₂ nanoparticles, thus giving rise to a mesoporous TiO₂/MWCNT hybrid texture. Notice that TiO₂ nanoparticles are well adhering to the CNT support.

According to the results, the enhanced photocatalytic effi-ciency of the composite for MB degradation has been explained according to the remarkable role played by MWCNTs, which act as pore-formers (medium-large mesopores), adsorbents, dispersing agents and electron reservoirs to trap electrons from TiO₂ particles due to UV irradiation, and hence hindering electron–hole pair recombination.

By taking into account mechanical/thermal stability together with the magnetic properties of the steel support, the move-ment from MWCNT to TiO₂/MWCNT hybrid scaffolds changes the surface properties from being hydrophobic to hydrophilic in nature.

Moreover, the hybrid character of the nanostructured scaf-fold, well anchored to the withstanding support, together with its porosity and the magnetic nature of the entire composite, can make it suitable for the controllable processing of water photodegradation for environmental remediation. In fact, magnetically driven TiO₂/MWCNT/steel composite has been shown to be very effective in a continuous photocatalytic test due to its recyclability.

Some additional optical and electrical properties of the TiO₂/ MWCNT hybrid system and of the MWCNT porous scaffold/ support may be taken under consideration to fabricate new functional structures, like sensors and energy materials.

Fig. 7   A picture representing the multifunctional properties of the TiO₂/MWCNT/steel composite.

Acknowledgements

Notes and references

1 I. Cobo, M. Li, B. S. Sumerlin and S. Perrier, *Nat. Mater.*, 2015, **14**, 143–159.

2 O. Kozachuk, I. Luz, F. X. Llabrés I Xamena, H. Noei, M. Kauer, H. B. Albada, E. D. Bloch, B. Marler, Y. Wang, M. Muhler and R. A. Fischer, *Angew. Chem., Int. Ed.*, 2014, **53**, 7058–7062.

3 M. J. Uddin, D. E. Daramola, E. Velasquez, T. J. Dickens, J. Yan, E. Hammel, F. Cesano and O. I. Okoli, *Phys. Status Solidi RRL*, 2014, **8**, 898–903.

4 S. Cravanzola, G. Haznedar, D. Scarano, A. Zecchina and F. Cesano, *Carbon*, 2013, **62**, 270–277.

5 S. Cravanzola, L. Muscuso, F. Cesano, G. Agostini, A. Damin, D. Scarano and A. Zecchina, *Langmuir*, 2015, **31**, 5469–5478.

6 M. M. Rahman, F. Cesano, F. Bardelli, D. Scarano and A. Zecchina, *Catal. Today*, 2010, **150**, 84–90.

7 F. Cesano, D. Scarano, S. Bertarione, F. Bonino, A. Damin, S. Bordiga, C. Prestipino, C. Lamberti and A. Zecchina, *J. Photochem. Photobiol., A*, 2008, **196**, 143–153.

8 G. Abellán, J. L. Jordá, P. Atienzar, M. Varela, M. Jaafar, J. Gómez-Herrero, F. Zamora, A. Ribera, H. García and E. Coronado, *Chem. Sci.*, 2015, **6**, 1949–1958.

9 T. Rodenas, I. Luz, G. Prieto, B. Seoane, H. Miro, A. Corma, F. Kapteijn, F. X. Llabrés i Xamena and J. Gascon, *Nat. Mater.*, 2014, **14**, 48–55.

10 C. Cheng, A. Amini, C. Zhu, Z. Xu, H. Song and N. Wang, *Sci. Rep.*, 2014, **4**, 4181.

11 L. Yang, S. Luo, S. Liu and Q. Cai, *J. Phys. Chem. C*, 2008, **112**, 8939–8943.

12 Y. Yao, G. Li, S. Ciston, R. M. Lueptow and K. A. Gray, *Environ. Sci. Technol.*, 2008, **42**, 4952–4957.

13 K. Woan, G. Pyrgiotakis and W. Sigmund, *Adv. Mater.*, 2009, **21**, 2233–2239.

14 Z. Peining, A. S. Nair, Y. Shengyuan, P. Shengjie, N. K. Elumalai and S. Ramakrishna, *J. Photochem. Photobiol., A*, 2012, **231**, 9–18.

15 F. Alosfur, M. H. Haji Jumali, S. Radiman, N. J. Ridha, M. A. Yarmo and A. A. Umar, *Int. J. Electrochem. Sci.*, 2013, **8**, 2977–2982.

16 F. Cesano, D. Pellerej, D. Scarano, G. Ricchiardi and A. Zecchina, *J. Photochem. Photobiol., A*, 2012, **242**, 51–58.

17 J. Matos, J. Laine and J. M. Herrmann, *Appl. Catal., B*, 1998, **18**, 281–291.

18 C. Y. Yen, Y. F. Lin, C. H. Hung, Y. H. Tseng, C. C. Ma, M. C. Chang and H. Shao, *Nanotechnology*, 2008, **19**, 045604.

19 G. Jiang, X. Zheng, Y. Wang, T. Li and X. Sun, *Powder Technol.*, 2011, **207**, 465–469.

20 B. Gao, G. Z. Chen and G. Li Puma, *Appl. Catal., B*, 2009, **89**, 503–509.

21 S. Da Dalt, A. K. Alves and C. P. Bergmann, *Mater. Res. Bull.*, 2013, **48**, 1845–1850.

22 Y. Dong, D. Tang and C. Li, *Appl. Surf. Sci.*, 2014, **296**, 1–7.

23 J. Matos, A. García, L. Zhao and M. M. Titirici, *Appl. Catal., A*, 2010, **390**, 175–182.

24 D. G. Shchukin, J. H. Schattka, M. Antonietti and R. A. Caruso, *J. Phys. Chem. B*, 2003, **107**, 952–957.

25 N. Lakshminarasimhan, E. Bae and W. Choi, *J. Phys. Chem. C*, 2007, **111**, 15244–15250.

26 R. A. Caruso, A. Susha and F. Caruso, *Chem. Mater.*, 2001, **13**, 400–409.

27 F. Cesano, S. Bertarione, A. Damin, G. Agostini, S. Usseglio, J. G. Vitillo, C. Lamberti, G. Spoto, D. Scarano and A. Zecchina, *Adv. Mater.*, 2008, **20**, 3342.

28 F. Cesano, S. Bertarione, M. J. Uddin, G. Agostini, D. Scarano and A. Zecchina, *J. Phys. Chem. C*, 2011, **114**, 169–178.

29 Z. B. Lei, J. M. Li, Y. X. Ke, Y. G. Zhang, H. C. Zhang, F. Q. Li and J. Y. Xing, *J. Mater. Chem.*, 2001, **11**, 2930–2933.

30 A. S. Nair, Z. Peining, V. J. Babu, Y. Shengyuan and S. Ramakrishna, *Phys. Chem. Chem. Phys.*, 2011, **13**, 21248–21261.

31 D. G. Shchukin and R. A. Caruso, *Chem. Mater.*, 2004, **16**, 2287–2292.

32 J. Shi, C. Sun, M. B. Starr and X. Wang, *Nano Lett.*, 2011, **11**, 624–631.

33 F. Sordello, C. Duca, V. Maurino and C. Minero, *Chem. Commun.*, 2011, **47**, 6147–6149.

34 Y. D. Xia and R. Mokaya, *J. Mater. Chem.*, 2005, **15**, 3126–3131.

35 J. G. Yu, H. T. Guo, S. A. Davis and S. Mann, *Adv. Funct. Mater.*, 2006, **16**, 2035–2041.

36 F. Cesano, G. Agostini and D. Scarano, *Thin Solid Films*, 2015, **590**, 200–206.

37 C. Aprile, A. Corma and H. Garcia, *Phys. Chem. Chem. Phys.*, 2008, **10**, 769–783.

38 J. N. Kondo, T. Yamashita, K. Nakajima, D. Lu, M. Hara and K. Domen, *J. Mater. Chem.*, 2005, **15**, 2035–2040.

39 J. H. Pan, Z. Lei, W. I. Lee, Z. Xiong, Q. Wang and X. S. Zhao, *Catal. Sci. Technol.*, 2012, **2**, 147–155.

40 E. Ortel, S. Sokolov and R. Kraehnert, *Microporous Mesoporous Mater.*, 2010, **127**, 17–24.

41 J. Shang, W. Li and Y. Zhu, *J. Mol. Catal. A: Chem.*, 2003, **202**, 187–195.

42 S. Sokolov, E. Ortel and R. Kraehnert, *Mater. Res. Bull.*, 2009, **44**, 2222–2227.

43 S. Sokolov, E. Ortel, J. Radnik and R. Kraehnert, *Thin Solid Films*, 2009, **518**, 27–35.

44 M. A. Anderson, A. L. Cudero and J. Palma, *Electrochim. Acta*, 2010, **55**, 3845–3856.

45 L. Camilli, M. Scarselli, S. Del Gobbo, P. Castrucci, F. Nanni, E. Gautron, S. Lefrant and M. de Crescenzi, *Carbon*, 2011, **49**, 3307–3315.

46 Y. Chen, Z. Lv, J. Xu, D. Peng, Y. Liu, J. Chen, X. Sun, C. Feng and C. Wei, *J. Power Sources*, 2012, **201**, 136–141.

47 S. Minnikanti, P. Skeath and N. Peixoto, *Carbon*, 2009, **47**, 884–893.

48 J. J. Moore, J. H. Kang and J. Z. Wen, *Mater. Chem. Phys.*, 2012, **134**, 68–73.

49 N. Sano, Y. Hori, S. Yamamoto and H. Tamon, *Carbon*, 2012, **50**, 115–122.

50 L. Camilli, P. Castrucci, M. Scarselli, E. Gautron, S. Lefrant and M. de Crescenzi, *J. Nanopart. Res.*, 2013, **15**, 1846.

51 L. Camilli, M. Scarselli, S. Del Gobbo, P. Castrucci, F. R. Lamastra, F. Nanni, E. Gautron, S. Lefrant, F. D'Orazio, F. Lucari and M. de Crescenzi, *Carbon*, 2012, **50**, 718–721.

52 C. T. Wirth, B. C. Bayer, A. D. Gamalski, S. Esconjauregui, R. S. Weatherup, C. Ducati, C. Baehtz, J. Robertson and S. Hofmann, *Chem. Mater.*, 2012, **24**, 4633–4640.

53 F. Cesano, I. Rattalino, F. Bardelli, A. Sanginario, A. Gianturco, A. Veca, C. Viazzi, P. Castelli, D. Scarano and A. Zecchina, *Carbon*, 2013, **61**, 63–71.

54 R. P. Vidano, D. B. Fischbach, L. J. Willis and T. M. Loehr, *Solid State Commun.*, 1981, **39**, 341–344.

55 G. Cravotto, D. Garella, E. Calcio Gaudino, F. Turci, S. Bertarione, G. Agostini, F. Cesano and D. Scarano, *New J. Chem.*, 2011, **35**, 915–919.

56 J. H. Lehman, M. Terrones, E. Mansfield, K. E. Hurst and V. Meunier, *Carbon*, 2011, **49**, 2581–2602.

57 M. S. Shamsudin and S. M. Sanip, *Adv. Mater. Res.*, 2015, **1109**, 509–513.

58 E. F. Antunes, A. O. Lobo, E. J. Corat, V. J. Trava-Airoldi, A. A. Martin and C. Veríssimo, *Carbon*, 2006, **44**, 2202–2211.

59 W. Li, H. Zhang, C. Wang, Y. Zhang, L. Xu, K. Zhu and S. Xie, *Appl. Phys. Lett.*, 1997, **70**, 2684–2686.

60 F. Cesano, M. M. Rahman, S. Bertarione, J. G. Vitillo, D. Scarano and A. Zecchina, *Carbon*, 2012, **50**, 2047–2051.

61 M. J. Uddin, F. Cesano, F. Bonino, S. Bordiga, G. Spoto, D. Scarano and A. Zecchina, *J. Photochem. Photobiol., A*, 2007, **189**, 286–294.

62 B. Gao, G. Z. Chen and G. Li Puma, *Appl. Catal., B*, 2009, **89**, 503–509.

63 B. Gao, C. Peng, G. Z. Chen and G. Li Puma, *Appl. Catal., B*, 2008, **85**, 17–23.

64 Y. Yu, J. C. Yu, J. G. Yu, Y. C. Kwok, Y. K. Che, J. C. Zhao, L. Ding, W. K. Ge and P. K. Wong, *Appl. Catal., A*, 2005, **289**, 186–196.

65 D. Y. Lee, C. Y. Shin, S. J. Yoon, H. Y. Lee, W. Lee, N. K. Shrestha, J. K. Lee and S. H. Han, *Sci. Rep.*, 2014, **4**, 3930.

66 A. Stevanovic, S. Ma and J. T. Yates, *J. Phys. Chem. C*, 2014, **118**, 23614–23620.

67 N. K. Shrestha, J. M. Macak, F. Schmidt-Stein, R. Hahn, C. T. Mierke, B. Fabry and P. Schmuki, *Angew. Chem.*, 2009, **121**, 987–990.

Development of multifunctional TiO$_2$/MWCNT hybrid composite grafted on stainless-steel grating.

Sara Cravanzola[a], Sagar M. Jain[a,b], Federico Cesano[a]*, Alessandro Damin[a] and Domenica Scarano[a]

[a] Department of Chemistry, NIS (Nanostructured Interfaces and Surfaces) Interdepartmental Centre and INSTM Centro Di Riferimento, University of Torino, Via P. Giuria, 7, 10125 Torino, Italy. *E-mail: federico.cesano@unito.it

[b] current address: sagarmjain@gmail.com.

Electronic Supplementary Information (ESI).

The morphology and the chemical analysis of the stainless steel grating are reported in Fig. S1. From the EDAX spectrum the chemical composition (Fe 66wt%, Cr 17.9 wt%, Ni 8 wt%, Si ≈0.4wt%) is obtained. The steel exhibits excellent withstanding properties, from the strong corrosion resistance to a wide range of atmospheric and chemical compounds to the excellent oxidation resistance (up to 900°C).

The BET surface area and the pore size distributions (PSDs) of the TiO$_2$/MWCNTs hybrid structure (obtained from the stainless steel support) and of the pure TiO$_2$ material (prepared by the same sol-gel and calcinations methods), as obtained from volumetric N$_2$ adsorption/desorption isotherms are shown in Fig. S2a,b

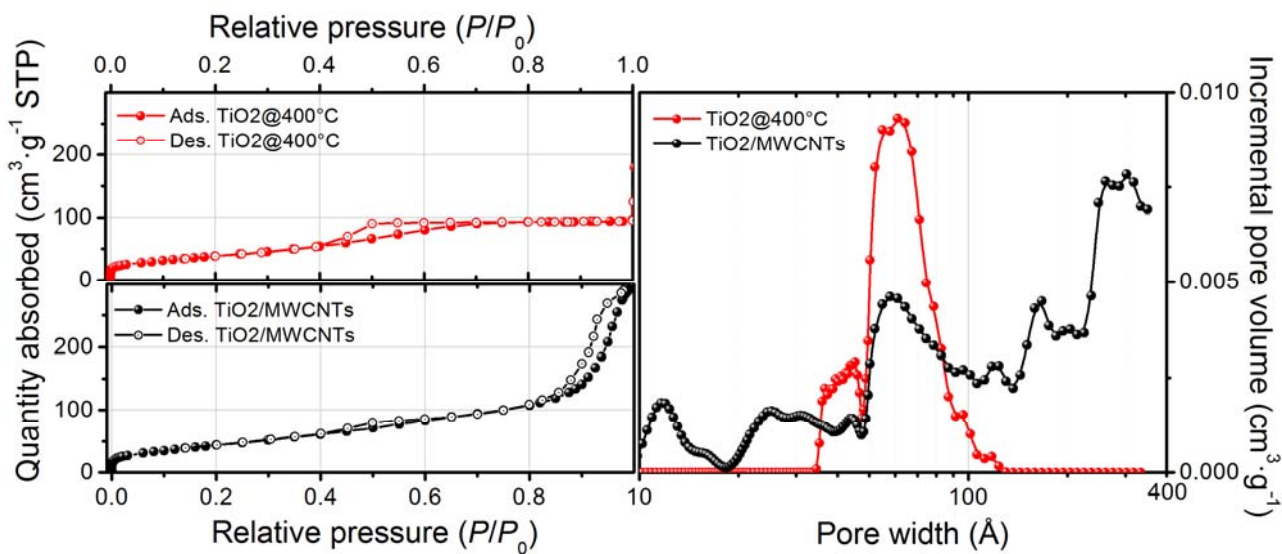In Fig. S3 the scheme of the structure of methylene blue along the three perpendicular directions is reported.

PL spectra of TiO$_2$/MWCNTs/stainless steel composite and of the discrete TiO$_2$ nanoparticles, obtained by adopting the same sol-gel preparation and treated at the same temperature are reported in Fig. S4.

The evolution of the surface properties (from the hydrophobic type of the MWCNTs/steel composite to the hydrophilic type of the TiO$_2$/MWCNTs/steel composite) is optically imaged in Fig. S5.

The quantities of TiO$_2$ and of MWCNTs of the composites have been obtained by means of the thermogravimetric profile upon isothermal oxidative conditions at 800°C (Fig. S6).
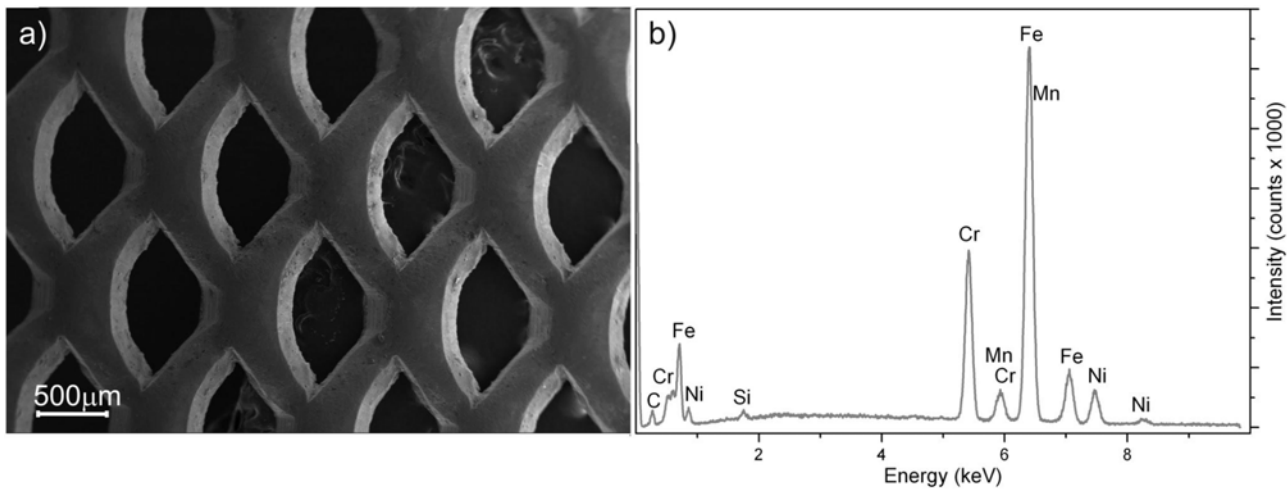
Fig. S1. A) SEM image and b) EDAX spectrum of the stainless steel grating used as a support.


Fig. S2. N_2-absorption/desorption isotherms (left panels) and pore size distributions (right panel) of the TiO_2 obtained at 400°C in air and of the TiO_2/MWCNT hybrid scaffold obtained from the stainless-steel support.
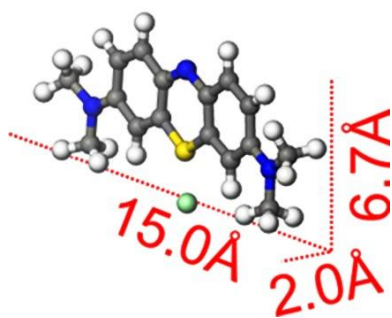
Fig. S3. Structure of methylene blue. The interatomic distances are reported along the three perpendicular directions.
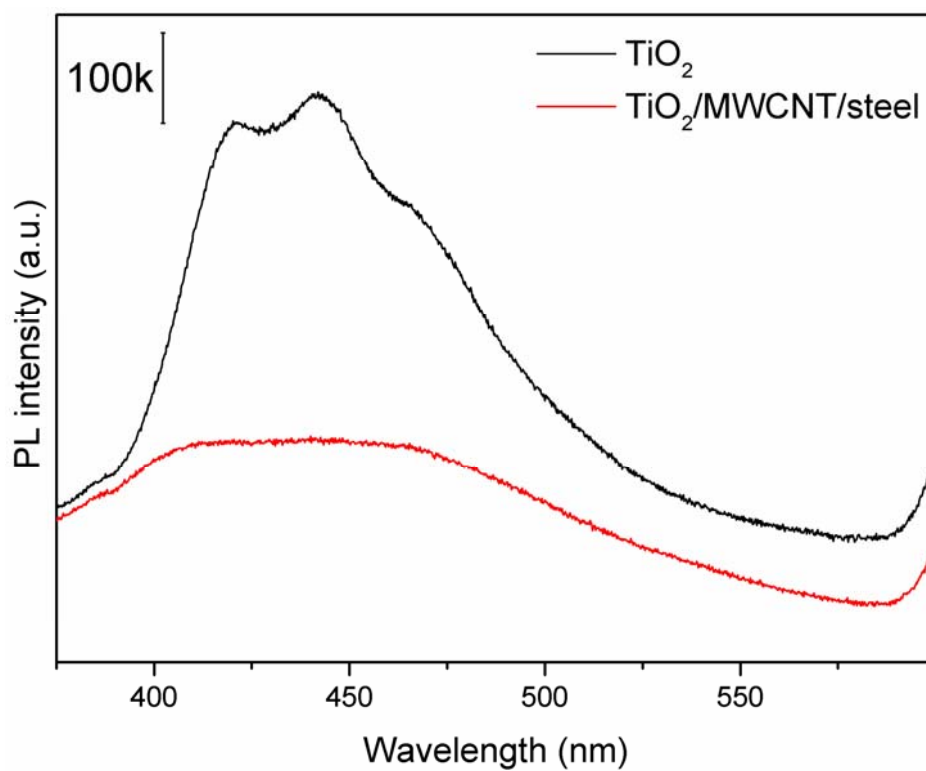
Fig. S4. PL emission spectra of TiO$_2$/MWCNTs/steel composite and of TiO$_2$ reference material (P25).
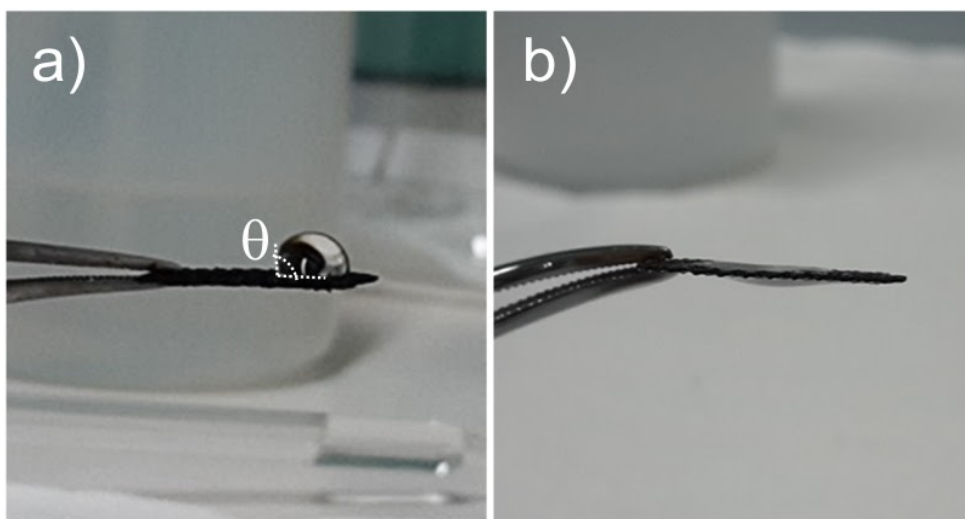
Fig. S5. Optical images showing the evolution of the surface properties (from hydrophobic type to hydrophilic type) of: a) the stainless steel grating covered by catalytically grown MWCNTs; and b) the same MWCNTs/steel composite coated with TiO_2.
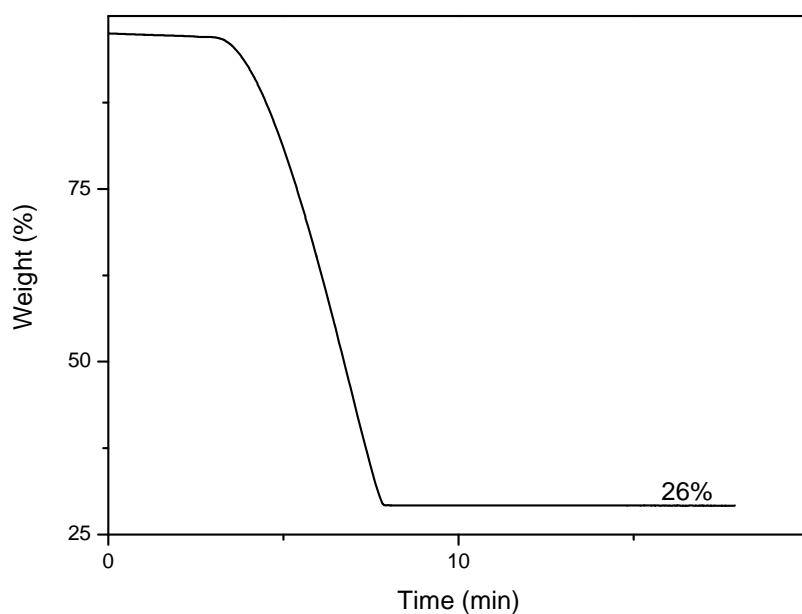
Fig. S6. Thermogravimetric profile of the TiO_2/MWCNTs/stainless steel grid under isothermal treatment at 800°C in air, after the heating in N_2 (ramp, stage 1).